

Simulation studies of GPS radio occultation measurements

G. Beyerle¹, M. E. Gorbunov², C. O. Ao³

G. Beyerle, GeoForschungsZentrum Potsdam (GFZ), Division 1, Kinematics and Dynamics of the Earth, Telegrafenberg, D-14473 Potsdam, Germany (e-mail: gbeyerle@gfz-potsdam.de)

M. E. Gorbunov, Institute for Atmospheric Physics, Moscow, Russia (e-mail: gorbunov@dkrz.de)

C. O. Ao, Jet Propulsion Laboratory, California Institute of Technology, Pasadena, USA

¹GeoForschungsZentrum Potsdam (GFZ),
Potsdam, Germany

²Institute for Atmospheric Physics,
Moscow, Russia

³Jet Propulsion Laboratory, California
Institute of Technology, Pasadena, USA

Abstract. The atmospheric propagation of GPS signals under multipath conditions and their detection are simulated. Using the multiple phase screen method C/A-code modulated L1 signals are propagated through a spherically symmetric refractivity field derived from a high-resolution radio sonde observation. The propagated signals are tracked by GPS receivers implemented in software and converted to refractivity profiles by the canonical transform technique and the Abel inversion. Ignoring noise and assuming an ideal receiver tracking behaviour the true refractivity profile is reproduced to better than 0.1% at altitude above 2 km. The non-ideal case is simulated by adding between 14 and 24 dB of Gaussian white noise to the signal and tracking the signal with receivers operating at 50 and 200 Hz sampling frequency using two different carrier phase detectors. In the upper troposphere and stratosphere the receiver models used in this study yield comparable refractivity profiles. However, in the mid-troposphere down to altitudes of about 2 km a Costas-type phase-locked loop tracking induces negative refractivity biases on the order of -1 to -2% at 50 Hz sampling frequency. Modifications to the receiver tracking algorithm significantly improves the retrieval results. In particular, replacing the Costas-loop's two-quadrant phase extractor with a four-quadrant discriminator reduces the refractivity biases by a factor of 5; increasing the sampling frequency from 50 to 200 Hz gains another factor of 2.

1. Introduction

Atmospheric soundings of temperature and water vapor by Global Positioning System (GPS) radio occultation (RO) measurements are increasingly being considered for numerical weather prediction and climate change studies. To-date a data set of more than 100,000 temperature profiles has been collected by the proof-of-concept GPS/Meteorology (GPS/MET) mission [Ware *et al.*, 1996] as well as the current CHAMP [Reigber *et al.*, 2000, 2002] and SAC-C missions. First validation studies based on CHAMP observations indicate that the observed temperature bias with respect to European Centre for Medium-Range Weather Forecasts (ECMWF) global analyses is less than 1 K above the tropopause and less than 0.5 K between 12 to 20 km at mid and high latitudes [Wickert *et al.*, 2001]. These values are consistent with validation results of GPS/MET data [Rocken *et al.*, 1997].

However, in the lower troposphere at mid and low latitudes a negative refractivity bias of more than 1% is observed in past and current RO data [see e.g., Rocken *et al.*, 1997; Marquardt *et al.*, 2001]. The negative bias is commonly attributed to the receivers' inadequate signal tracking behavior within zones of multipath signal propagation [see e.g., Gorbunov, 2002b]. These multipath zones are caused by complicated structures in the tropospheric refractivity field generated by spatial variations of the water vapor distribution. The analysis of radio occultation data affected by multipath propagation is extensively discussed in the literature [Gorbunov *et al.*, 1996; Karayel and Hinson, 1997; Hocke *et al.*, 1999]. Recently, the canonical transform (CT) method was devised to solve the problem of calculating bending angle pro-

files from phase and amplitude data observed within multipath regions [*Gorbunov et al.*, 2000; *Gorbunov*, 2002*a*, *b*]. CT processing of a large number of GPS/MET and CHAMP observations, however, did not succeed in removing the refractivity bias suggesting that the quality of the lower tropospheric data is degraded. This conclusion is corroborated by a sliding spectral analysis [*Gorbunov*, 2002*b*].

The present study investigates the observed refractivity bias using end-to-end simulations. The atmospheric propagation of a C/A-code modulated GPS signal is modelled. For simplicity only the neutral atmosphere is considered in the following, dispersion due to ionospheric propagation is not taken into account. GPS signal demodulation is performed by multiplication with a C/A-code replica. In multipath zones, however, the signal cannot be demodulated unambiguously since multiple interfering rays may have different phase delays and Doppler shifts. The objective of the present study is to investigate the influence of the receiver tracking process on retrieved amplitude and phase data and explore their relation to the negative refractivity bias.

The paper is organized into two parts: first, the methods employed in the simulation chain are introduced and described. Briefly reviewed are the multiple phase screen method which is used to simulate GPS signal propagation through the atmosphere and the CT method which transforms the amplitude and phase data into bending angle profiles; the receiver tracking module is discussed in more detail. Second, the simulation studies are described and the results are discussed.

In our simulation study the refractivities retrieved at altitude ranges between 2 and 6 km differ characteristically from values above 6 km and below about 2 km. For brevity we denote the altitude range between 2 and 6 km as “mid-troposphere”, whereas the altitude range below 2 km is termed “lower troposphere.”

2. Method

The atmospheric propagation of GPS signals, the tracking process by a receiver instrument and the data analysis is studied using a sequence of simulation elements. Each element processes the output of the previous element and generates the input of the following element. This simulation “chain” is schematically illustrated in Fig. 1.

Using the multiple phase screen (MPS) method the atmospheric propagation of a C/A-code modulated GPS signal based on high-resolution refractivity profiles $N(\vec{r}) = (n(\vec{r}) - 1) \cdot 10^6$ is modeled. Here, $n(\vec{r})$ denotes the real refractive index. The refractivity field is assumed to be spherically symmetric, i.e. $N(\vec{r}) = N(r)$. The generated electromagnetic (EM) field serves as input to a single channel GPS software receiver. The receiver’s output data, carrier phases and signal-to-noise ratios (SNRs), are converted to bending angle profiles using the CT method. Finally, refractivity profiles are obtained by Abel-transforming the bending angle profiles thereby closing the simulation loop. Statistical analyses of original (true) and retrieved refractivity profiles provide insight into systematic deviations introduced by the individual simulation steps.

In the following subsections the individual simulation elements are described.

2.1. Multiple phase screen simulation

Atmospheric propagation of GPS signals is numerically simulated using the multiple phase screen (MPS) technique [Knepp, 1983; Martin and Flatté, 1988]. Several studies simulating radio occultation observations successfully employed the MPS technique [see e.g., Karayel and Hinson, 1997; Gorbunov and Gurvich, 1998]. Since the spatial scales of the refractive index field variations are much larger than the GPS signal wavelength (19.03 cm at L1) backscattering can be ignored and the propagated signal can be determined by representing the continuous medium by a sequence of phase screens. For simplicity, we model an infinitely remote GPS satellite immovable with respect to the Earth's atmosphere. The incident wave is a plane wave with a unit amplitude.

Within the MPS approach the atmospheric refractivity field $N(r)$ is modelled as a series of phase screens; Fig. 2 illustrates the concept and defines the coordinate system. At each screen the incident EM wave suffers a phase shift whereas the wave's amplitude remains unchanged. Between the screens the EM wave is propagated through vacuum. The result of the MPS calculation is the signal amplitude $A(y)$ and phase $\phi(y)$ on the observation screen O .

The phase screens are oriented parallel to each other; thus, the numerical calculation of the vacuum propagation can be implemented efficiently on the basis of fast Fourier transformations [Goodman, 1968]. For brevity we refrain from quoting the MPS equations in detail; descriptions of the MPS method can be found in Knepp [1983], Martin and Flatté [1988], Karayel and Hinson [1997] and Sokolovskiy [2001].

The GPS signal's spread-spectrum modulation implies that the transmitter signal $u_i(t)$ arriving at the first phase screen is not a pure tone but exhibits a finite bandwidth [Kaplan, 1996]. As an illustration the main lobe and the first few ancillary lobes of a normalized power spectral density calculated from a L1 signal modulated with C/A-code PRN 17 is shown in Fig. 3. The main lobe extends from about $f_c - 1.1$ Mhz to $f_c + 1.1$ Mhz; here, f_c denotes the L1 carrier frequency of 1576.52 MHz. For simplicity we treat only C/A-code modulation and ignore the effects from P-code and the 50 Hz navigation data modulation [Kaplan, 1996].

The C/A-code consists of a pseudo-random sequence of 1023 bits (chips), $CA_i = \pm 1$ with $i = 1, \dots, 1023$ and is periodic with a repeat frequency of 1 kHz (ignoring Doppler shifts due to relative motion between transmitter and receiver). Thus, $u_i(t)$ exhibits a discrete power spectrum with individual spectral lines separated by $\Delta f = 1$ kHz,

$$u_i(t) = \sum_{n=N_c-N^*}^{N_c+N^*} c_n \exp [2\pi i (f_c + n \Delta f) t] . \quad (1)$$

Here, $N_c = f_c / \Delta f = 1,576,200$ and N^* is defined below. The coefficients c_n are obtained by evaluating the Fourier integral and are found to be

$$c_n = \begin{cases} \frac{1}{1023} \sum_{k=1}^{1023} CA_k & : n = N_c \\ \frac{\sin\left(\frac{\pi(N_c - n)}{1023}\right)}{\pi(N_c - n)(-1)^{(N_c - n)}} \sum_{k=1}^{1023} CA_k \exp\left(i \frac{\pi(N_c - n)}{1023} (2k - 1)\right) & : n \neq N_c \end{cases} \quad (2)$$

The propagation of the C/A-modulated signal is simulated by performing a series of MPS calculations using plane waves with frequencies varying between $f_c - 1.1$ MHz and $f_c + 1.1$ MHz roughly covering the first main lobe, i.e. we choose $N^* \equiv 1100$.

MPS simulations for monochromatic signals are very fast. However, the propagation of $2N^* + 1 = 2201$ components is computationally expensive. Therefore, the number of frequency components is reduced to 129 and the MPS amplitudes and phases, $A_n(y)$ and $\phi_n(y)$, $n = (N_c - N^*, \dots, N_c + N^*)$, are obtained by linear interpolation. Finally, the signal $u_o(y, t)$ at observation screen position y is assembled from the individual spectral components according to

$$u_o(y, t) = \sum_{n=N_c-N^*}^{N_c+N^*} A_n(y) \exp(i \phi_n(y)) c_n \exp[2\pi i (f_c + n \Delta f) t] . \quad (3)$$

In the following we assume that the receiver moves with a constant velocity $v = y/t \equiv 2.7$ km/s along the observation screen corresponding to a LEO satellite orbit altitude of about 450 km. The observed GPS signal, therefore, is $u_r(y) \equiv u_o(y, t = y/v)$

2.2. Receiver simulation

The simulated GPS signals $u_r(t)$ are processed by a receiver module implemented in software. For simplicity it is designed as a single channel receiver and is restricted to C/A-code tracking only; decoding of navigation data bits is not implemented. Here we focus on specific aspects of the simulation receiver relevant to this study; for detailed discussions of GPS receiver technology we refer to the literature [*Kaplan*, 1996; *Parkinson and Spilker*, 1996; *Tsui*, 2000].

Typical GPS signal levels found in antenna phase centers of ground-based or LEO-based receivers are on the order of -130 dBm, about -19 dB below the noise floor of -111 dBm [*Kaplan*, 1996; *Tsui*, 2000]. We model the receiver's input as the sum

of simulated signal $u_r(t)$ and white Gaussian noise. In our simulation runs signal-to-noise ratios of -14 dB (strong signal) and -24 dB (weak signal) are used.

The receiver itself consists of two parts, the front-end and the code/carrier tracking loops. The front-end performs down-conversion of the received signal from L1-band at $f_c = 1575.42$ MHz to an intermediate frequency. Down-conversion is achieved by direct sampling, i.e. by sampling at a smaller rate than the carrier frequency f_c [Tsui, 2000]. We choose $f_s = 5.045$ MHz; thus, the L1 signal centered at f_c is aliased to a frequency range centered at the intermediate frequency of $f_d = 1.38$ MHz.

The samples are digitized with a three-level discriminator, quantization thresholds are ± 0.61 times the noise's standard deviation [Thomas, 1995]. The digitized samples are tracked with two Costas phase-locked loops (PLL), the code and the carrier tracking loop. Fig. 4 shows a schematic diagram of the two connected loops. The PLLs compensate changes in carrier and code frequency due to delays induced by the atmospheric refractivity field (and possible relative motions between transmitter and receiver). The modulation-free carrier, required for PLL carrier tracking, is obtained by multiplying the received signal with a C/A-code model produced by the code tracking loop. Similarly, the code tracking loop inputs a carrier-free signal. In the carrier loop the demodulated signal is multiplied with sine and cosine values generated by a numerically controlled oscillator (NCO) and the result is low-pass filtered by summing over a large number of samples. Typical summation periods (predetection integration times) are 10 or 20 ms; thus the sum extends over $10 \text{ ms} \cdot f_s = 50,450$ or $20 \text{ ms} \cdot f_s = 100,900$ samples. Similar to the carrier tracking loop, the code tracking

PLL reads carrier-free signals which are obtained by multiplying the received signal with a cosine wave produced by the carrier tracking loop. The carrier-free signal then is multiplied with C/A-code replicas shifted by one half-chip (corresponding to a time offset of about $\pm 0.5 \mu\text{s}$). In general, the tracking behavior of second order PLLs are characterized by loop gain G , bandwidth B_n and damping ratio ζ [*Gardner*, 1979; *Stensby*, 1997]; the parameter values used in this study are listed in Table 1 [*Tsui*, 2000].

Within multipath propagation zones the signal phase exhibits strong fluctuations (cf. Fig. 8 bottom panel, between -35 and -25 km). Thus, significant deviations between observed and model signal, denoted as phase error \mathcal{E} , occur and need to be detected reliably by the carrier tracking loop. \mathcal{E} is related to the in-phase component I and quadrature-phase component Q , the outputs of the two carrier PLL low-pass filters, according to [*Kaplan*, 1996]

$$\mathcal{E} = \arctan\left(\frac{Q}{I}\right). \quad (4)$$

(We note that in the literature [e.g. *Kaplan*, 1996] approximations to Eqn. 4 are given which are computationally less demanding. However, these approximations suffer from large deviations already at moderate values of \mathcal{E} and therefore will not be considered here.)

The characteristic feature of Costas PLLs is their insensitivity with respect to 180° phase changes; in particular, the phase correction \mathcal{E} remains unchanged if I and Q change their sign, i.e. $\mathcal{E}(I, Q) = \mathcal{E}(-I, -Q)$. As a consequence, the 50 Hz navigation message modulation does not impair operation of the Costas loop provided the sample

summation does not straddle data bit boundaries. However, the Costas loop is less attractive if the carrier exhibits phase fluctuation exceeding 90° . Phase deviation larger than 90° are aliased into the $[-90^\circ, 90^\circ]$ interval; e.g. a phase deviation of 135° produces a phase correction of -45° causing the NCO to decrease its frequency instead of increasing it.

In order to improve the carrier loop's tracking behavior within multipath zones we tentatively replaced the two-quadrant arctangent phase detector $\arctan(Q/I)$ (Eqn. 4) by a four-quadrant arctangent extractor $\arg(I, Q)$ defined as

$$\arg(x, y) = \begin{cases} \arctan\left(\frac{y}{x}\right) & : x > 0 \\ \arctan\left(\frac{y}{x}\right) + \pi & : x < 0 \text{ and } y \geq 0 \\ \arctan\left(\frac{y}{x}\right) - \pi & : x < 0 \text{ and } y < 0 \\ \pi/2 & : x = 0 \text{ and } y > 0 \\ -\pi/2 & : x = 0 \text{ and } y < 0 \\ 0 & : x = 0 \text{ and } y = 0 \end{cases} \quad (5)$$

For phase errors \mathcal{E} between -90° and 90° the \arg phase extractor gives the same result as the two-quadrant arctangent extractor. However, it also yields the correct values for phase angles between -180° and -90° and between 90° and 180° where the two-quadrant arctangent extractor deviates by $\pm 180^\circ$. Thus, the \arg phase extractor extends the valid phase range from $\pm 90^\circ$ to $\pm 180^\circ$. The drawback is that a carrier loop with an \arg phase extractor no longer is insensitive with respect to phase reversals due to the navigation message modulation. The navigation message thus needs to be removed in advance from the incoming signal by a process called “data wipeoff” [Kaplan, 1996].

The receiver outputs are I and Q components at the C/A-code period of nominally 1 msec. From these values signal-to-noise ratios (SNR) are obtained

$$SNR = \frac{1}{N} \sqrt{\left(\sum_k^N I_k\right)^2 + \left(\sum_k^N Q_k\right)^2}, \quad (6)$$

at 50 Hz ($N = 20$) or 200 Hz ($N = 10$); the carrier phase is obtained from the carrier loop's NCO phase.

2.3. Canonical transform technique

The next step in the simulation procedure involves the derivation of bending angle profiles from phase and SNR data produced by the software GPS receiver. The refractivity profile considered in this study (see Fig. 7) induces strong multipath beam propagation. As a result the EM field's phases and amplitudes exhibit strong fluctuation at the observation screen as is illustrated in Fig. 8.

A schematic representation of multipath beam propagation is shown Fig. 5. The projection of the ray manifold onto the (x, y) -plane (occultation plane in geometrical space) illustrates a ray structure caused by a strongly refracting atmospheric layer. Between t_1 and t_2 a receiver following the LEO orbit detects signals contributions from several interfering rays.

The canonical transform (CT) method solves the problem of calculating the bending angle $\epsilon(p)$ as a function of ray impact parameter p within multipath regions. A detailed and motivated description of the method is given by *Gorbunov* [2001, 2002a, b].

The CT method uses the connection between geometrical optics and wave optics. In geometrical optics rays are described by the canonical Hamilton system which

defines the evolution of coordinate y and corresponding momentum η . η is equal to the angle between the ray direction and the x -axis. The propagation distance x is looked at as the temporal coordinate. Multipath propagation is characterized by the fact that multiple rays may have the same coordinate y . In geometrical optics we can introduce a new coordinate and momentum by means of a canonical transform. If we take the ray impact parameter p as the new coordinate, then the canonical transform can be written in the form

$$p = -\eta x + y \sqrt{1 - \eta^2} \quad (7)$$

$$\xi = \arcsin \eta .$$

This transform from the old canonical coordinates (y, η) to the new ones (p, ξ) resolves multipath propagation, because, for a spherically symmetrical medium, ray impact parameters p are different for different rays. In wave optics we consider the wave field as a function of x and y , which we denote $u_x(y)$. The corresponding transform of the wave function to the new representation is given by the following Fourier integral operator

$$\check{u}_x(p) = \frac{k}{2\pi} \int d\eta (1 - \eta^2)^{\frac{1}{4}} \exp \left(ik \left(p \arcsin \eta - x \sqrt{1 - \eta^2} \right) \right) \mathcal{F}[u_x](\eta) \quad (8)$$

where $\mathcal{F}[u_x](\eta)$ denotes the Fourier transform of $u_x(y)$

$$\mathcal{F}[u_x](\eta) = \int dy \exp(-i k y \eta) u_x(y) . \quad (9)$$

and $k = 2\pi/\lambda$ is the vacuum wave number. Because in this representation we have single-ray propagation, the momentum ξ is equal to the derivative of the optical path

of the transformed wave function. The bending angle $\epsilon(p)$ follows from

$$\begin{aligned}\epsilon(p) &= -\xi(p) + \epsilon_0(p) \\ &= -\frac{1}{k} \frac{d}{dp} \arg(\check{u}_x(p)) + \epsilon_0(p) \\ \epsilon_0(p) &= -\arcsin\left(\frac{x_G p + r_E \sqrt{x_G^2 + r_E^2 - p^2}}{r_E^2 + x_G^2}\right).\end{aligned}\tag{10}$$

where $\epsilon_0(p)$ is the initial direction angle at the GPS satellite. (x_G, y_G) and r_E denote the position of the GPS satellite and the local curvature radius of Earth's surface, respectively.

Fig. 5 shows a graphical illustration of the ray manifold in the three-dimensional (x, y, p) -space. The orbit segment in the (p, x) -plane deviates significantly from the near-circular shape in geometrical space.

The squared magnitude of the transformed field in impact parameter space, or the CT-amplitude, describes the energy distribution in the impact parameter space. For a spherically symmetrical atmosphere without absorption this function is a constant in the light zone and it drops abruptly to very small values in the shadow zone. In order to illustrate this property CT-amplitudes are computed for a simulated EM field obtained by MPS calculations. Spatial filters are applied to the field resulting in signals $w(y)$; for simplicity the filter shape is taken to be a rectangular window, i.e.

$$w(y) = \begin{cases} u(y) & : y^* - \Delta y/2 < y < y^* + \Delta y/2 \\ 0 & : \text{else} \end{cases}\tag{11}$$

Two signals are calculated using $y^* = -15$ km and $y^* = -25$ km, the corresponding CT-amplitudes $|\check{w}_x(p)|$ are shown in Fig. 6. In both cases the window width Δy is

2 km. At $y^* = -15$ km single ray propagation dominates and the observed signal is mainly determined by rays which have probed the atmosphere at ray heights of about 8 km (about 6 km altitude). However, the signals observed around $y^* = -25$ km contain contributions from two height ranges, one at 6.5 km ray height (4.5 km altitude) and the other in the lower troposphere at 4.5 km ray height (2.5 km altitude). Thus, at $y^* = -25$ km the receiver resides within a multipath zone. The implications will be discussed below. In the following ray height is defined as $h = p - r_E$. (Typically, ray heights are about 2 km larger than the corresponding tangent altitudes.)

2.4. Abel transform

Finally, the bending angle profiles $\alpha(p)$ are inverted back into refractivity profiles $N(r)$ using the Abel transform [Lindal *et al.*, 1987; Melbourne *et al.*, 1994; Kursinski *et al.*, 1996; Hocke *et al.*, 1999]. The Abel transform is the last step in the simulation chain.

3. Discussion of simulation results

The simulations are performed with a refractivity profile which is derived from a high-resolution radio sonde observation. The temperature and humidity measurement took place on the Atlantic ocean at 23.1°S, 26.0°W on 29 October 1996 between 12:00 and 14:00 UTC during the ALBATROS field measurement campaign aboard the research vessel “POLARSTERN”. The dominating source of error with respect to refractivity measured by the rawinsonde is the relative humidity (RH) sensor’s

accuracy of 2% RH and the sensor's precision of 1% RH [Vaisala, 1989]. In order to reduce the humidity measurement noise the refractivity profiles are smoothed with an 8 point running mean filter thereby reducing the vertical resolution from about 15 m to about 120 m. The sonde profile ends at an altitude of 26.3 km. Above that altitude the profile is continued by an exponential function using a scale height of 7.9 km. The profile, the tropospheric part of which is plotted in Fig. 7, was selected because of several layered humidity structures in the mid-troposphere which translate into corresponding layers in the vertical refractivity gradient. As will be shown below these layers cause multipath beam propagation in the lower and mid-troposphere.

From the refractivity profile signal amplitudes and phases on the observation screen are determined using the MPS technique. We choose the integration step and resolution according to *Sokolovskiy* [2001]. Each of the $L = 2001$ phase screen consists of $2^{19} = 524,288$ grid points with a separation of $\Delta y = 0.54$ m, vertically the screens extend over about 283 km. Horizontally, the 2001 phase screens are separated by a distance of $\Delta x = 1$ km covering a horizontal range of 2000 km. The distance between the last phase screen and the observation screen is 1500 km, the distance between central and observation screen therefore is 2500 km corresponding to a satellite orbit altitude of 450 km. As described in the previous section the MPS calculation is performed for 129 frequency components covering the main spectral lobe of the C/A-code spectrum.

Exemplarily an amplitude and Doppler profile as a function of observation plane position y at the carrier frequency of 1.57542 GHz is shown in Fig. 8. The profile

exhibits strong variations in Doppler frequency in particular at screen positions below -22 km.

White Gaussian noise is added to the derived MPS signal, the sum is three-level quantized and tracked by the software receiver. The process is repeated 100 times, at each case using the same signal only replacing the noise component. In each iteration the complete retrieval leading from signal amplitude and phase data to refractivity profiles are performed. Mean and standard deviations of CT-amplitudes, bending angles and refractivities are calculated from the profile ensemble. In addition, the MPS signal is processed directly omitting the receiver simulation step in order to quantify to what extend the receiver tracking influences the derived refractivity (“ideal receiver case”).

A large number of simulation runs have been performed; for brevity we restrict the discussion to four cases: in the baseline receiver experiment sampling frequency is taken to be 50 HZ and Costas-PLL carrier tracking (two-quadrant arctangent phase detector) is used, the SNR level is -14 dB. The results are compared to simulations with a four-quadrant arctangent phase detector, 200 Hz sampling and/or a larger noise level of -24 dB. The results are compiled in Figs. 9 to 12. Fig. 9 shows the result for the baseline experiment, Fig. 10 the result for a four-quadrant arctangent phase detector, Figs. 11 the result for a four-quadrant arctangent phase detector / 200 Hz sampling and Figs. 12 the result for a four-quadrant arctangent phase detector / 200 Hz sampling / -24 dB noise.

In all four figures the relative deviation between derived and true refractivity profile is plotted, 1-sigma standard deviations are marked in grey. Above 6 km altitude the retrievals agree to better than 0.3% (Fig. 9, 10 and 12), at 200 Hz the agreement improves and reaches 0.1% in the low noise case (Fig. 11). At altitudes between 2.5 and 6 km the two-quadrant phase detector tracking produces refractivity biases exceeding -1.5% with 50 Hz sampling frequency (Fig. 9). The bias is reduced by about a factor of five if the two-quadrant phase detector is replaced by the four-quadrant phase detector (Fig. 10); further improvement is obtained by increasing the sampling frequency from 50 to 200 Hz (Fig. 11). Even under weak signal conditions with SNR of -24 dB the four-quadrant phase detector outperforms the baseline receiver by about a factor of three in terms of the refractivity bias (Fig. 12). However, the standard deviation increases significantly indicating that loss of lock occurs more frequently below 6 km under low SNR conditions.

Within the planetary boundary layer below 2 km altitude the retrievals exhibit strong negative biases (Figs. 9 to 12). In all simulation experiments the bias increases strongly with decreasing altitude and reaches -25% at the surface (not shown). Ducting (confinement of the signal to a narrow region of the troposphere) is excluded as possible explanation since the vertical refractivity gradient never becomes smaller than the critical value of about -160 km^{-1} (cf. Fig. 7). An analysis similar to the one discussed in Fig. 6 shows that rays with tangent heights below 2 km strike the observation screen at locations below -40 km. However, below -40 km, in particular between -60 and -50 km, the GPS signal is characterized by low SNR as shown in

the top panel of Fig. 8. Thus, defocusing is the most likely cause responsible for the observed refractivity bias below 2 km.

The CT-amplitudes corresponding to Figs. 9–12 are plotted in Fig. 13. The CT-amplitude obtained from the ideal receiver simulation is shown as well; the latter follows closely the ideal step function shape indicating the beginning of the shadow zone at about 2.3 km ray height, whereas the Costas-loop receiver tracking results (Figs. 9) expose frequent drop-offs of the CT-amplitude by more than 50%. We note that similar amplitude variations appear in a large fraction of CT-amplitudes calculated from GPS/MET and CHAMP observations.

It was shown in Fig. 6 that the measurement taken around -25 km on the observation screen is largely determined by signals which probed the atmosphere at ray heights between 4–5 km (about 2–3 km altitude). Thus, differences between the two-quadrant phase extractor retrieval (Figs. 9) and the four-quadrant cases (Figs. 10 and 11) within the 2–3 km altitude region are expected to correspond to deviations in retrieved amplitudes and phases around $y = -25$ km. These frequency and amplitude deviations are indeed observed: in Figs. 14 and 15 the retrieved amplitude and Doppler profiles are compared with the true profiles as obtained from the MPS calculations. The Doppler and amplitude profiles show strong fluctuations which are characteristic for multipath signal propagation (c.f. Fig. 16). From Fig. 14 it is evident that the four-quadrant phase detector performs significantly better in resolving the fine structure of the Doppler profile, in particular between -24 and -25 km, than the baseline receiver using a Costas-PLL.

The deviations in Doppler frequency between the two tracking simulations (Fig. 14) are not matched by corresponding amplitude differences (Fig. 15). Despite their strong variability both receivers are able to follow the amplitude signatures closely with only small differences between the two tracking results. We note that the baseline's receiver normalized SNR rarely drops below 0.1 within the screen range considered here despite its poor Doppler tracking performance.

Finally, the optical path lengths obtained from a ray tracing calculation are plotted in Fig. 16 (dotted line) for comparison with the corresponding MPS profiles (dashed and solid lines). Multi-valued optical paths in the geometrical optics solution indicate the extent of multipath regions; e.g., between $y = -35$ km and $y = -24$ km the GPS receiver measures the interference pattern of two or more individual rays. The largest optical path difference between interfering rays are found to be about 7 m at $y = -24.5$ km corresponding to about 1/40 of the 300 m C/A-code chip length. In addition, the optical path differences obtained by MPS calculations including and excluding the receiver tracking are shown in Fig. 16 as well (dashed and solid line, respectively). Whereas the receiver reproduces the true MPS values up to a constant factor within regions of single ray propagation ($y > -24$ km), the tracking results start to deviate significantly within the multipath region (-35 km $< y < -24$ km).

4. Conclusions

Simulation studies of atmospheric signal propagation, receiver tracking and canonical transform data analysis were performed for a high-resolution refractivity profile

derived from a tropical radiosonde sounding. The study is based on the parabolic approximation of the electromagnetic wave equations, the assumption of spherical symmetry in the atmospheric refractivity field and the absence of absorption effects.

Within regions of multipath signal propagation interference between individual rays cause enhanced amplitude and Doppler frequency fluctuations. However, these fluctuations need to be mapped accurately in order to be able to reconstruct the bending angle profile within the framework of the canonical transform method.

From the simulation results we arrive at the following conclusions:

1. Simulations with a noise-free signal and an ideal receiver reproduce the true refractivity profile to better than 0.1% at altitude above 2 km.

2. Tracking with a baseline receiver model at 50 Hz sampling and using a standard Costas-type phase-locked loop tracking induces negative refractivity biases on the order of -1 to -2% in the mid-troposphere. These values are of the same order of magnitude as biases observed in current satellite missions.

3. In the mid troposphere the retrieved refractivity profiles depend on receiver tracking algorithms and parameters. By modifying receiver tracking algorithms the simulated retrievals could be improved significantly at altitudes between 2 and 6 km. In particular, replacing the two quadrant phase extractor with a four-quadrant discriminator reduced the refractivity biases by a factor of 5. Increasing the sampling frequency from 50 to 200 Hz gained another factor of 2.

4. At altitudes below 2 km an even larger negative refractivity bias is observed in all tracking experiments reaching -25% at the surface. Most likely this bias is caused by signal defocusing.

5. While the retrieved Doppler profiles differ significantly within multipath regions between different receiver models there is quite close agreement in the SNR data. Thus, in selecting tracking algorithms emphasis should be put on recovering the phase information; tracking of SNR is less critical.

In our study the atmosphere is assumed to be free from ducting layers, i.e., the vertical refractivity gradient dN/dz exceeds about -160 km^{-1} at all altitude levels. If, on the other hand, $dN/dz \lesssim -160 \text{ km}^{-1}$ the corresponding trapping layers cause a negative refractivity bias (C. O. Ao et al., manuscript in preparation and S. Sokolovskiy, Effect of the super refraction and small refractivity irregularities on inversions of radio occultation signals, Radio Occultation Science Workshop, August 21–23, 2002, Bolder, USA).

While the influence of the receiver algorithms on amplitude and phase data probably cannot be removed completely our simulation results suggest that improvements can be obtained by using a four-quadrant phase detector and by increasing the sampling frequency. These improvements come at the price of an increase in data volume and the added complexity of a “data wipeoff” implementation required for removing the 50 Hz navigation message modulation.

Acknowledgments. Helpful discussions with P. Hartl, C. Marquardt, T. Meehan, T. Schmidt and J. Wickert are gratefully acknowledged. We thank R. Weller, Alfred

Wegener Institute for Polar and Marine Research, Bremerhaven, Germany for high-resolution rawinsonde data. This study was carried out within the HGF project “GPS Atmospheric Sounding” (grant no. FKZ 01SF9922/2) lead by Ch. Reigber.

References

- Gardner, F. M., *Phaselock techniques*, John Wiley, New York, 1979.
- Goodman, J. W., *Introduction to Fourier optics*, McGraw-Hill, New York, 1968.
- Gorbunov, M. E., Radioholographic methods for processing radio occultation data in multipath regions, technical report 01-02, Danish Meteorological Institute, Copenhagen, <http://www.dmi.dk/f+u/publikation/vidrap/2001/Sr01-02.pdf>, 2001.
- Gorbunov, M. E., Canonical transform method for processing GPS radio occultation data in lower troposphere, *Radio Sci.*, *37*, 10.1029/2000RS002592, 2002*a*.
- Gorbunov, M. E., Radio-holographic analysis of Microlab-1 radio occultation data in the lower troposphere, *J. Geophys. Res.*, *107*, (D12), 10.1029/2001JD000889, 2002*b*.
- Gorbunov, M. E., and A. S. Gurvich, Microlab-1 experiment: Multipath effects in the lower troposphere, *J. Geophys. Res.*, *103*, (D12), 13,819–13,826, 1998.
- Gorbunov, M. E., A. S. Gurvich, and L. Bengtsson, Advanced algorithms of inversion of GPS/MET satellite data and their application to reconstruction of temperature and humidity, Report 211, Max-Planck-Institut für Meteorologie, Germany, Hamburg, 1996.

- Gorbunov, M. E., A. S. Gurvich, and L. Kornbluh, Comparative analysis of radioholographic methods of processing radio occultation data, *Radio Sci.*, *35*, (4), 1025–1034, 2000.
- Hocke, K., A. G. Pavelyev, O. I. Yakovlev, L. Barthes, and N. Jakowski, Radio occultation data analysis by the radioholographic method, *J. Atmos. Solar-Terr. Phys.*, *61*, (15), 1169–1177, 1999.
- Kaplan, E. D., *Understanding GPS, Principles and applications*, Artech House, Boston, London, 1996.
- Karayel, E. T., and D. P. Hinson, Sub-Fresnel-scale vertical resolution in atmospheric profiles from radio occultation, *Radio Sci.*, *32*, (2), 411–423, 1997.
- Knepp, D. L., Multiple phase-screen calculation of the temporal behaviour of stochastic waves, *Proc. of the IEEE*, *71*, (6), 722–737, 1983.
- Kursinski, E. R., G. A. Hajj, W. I. Bertiger, S. S. Leroy, T. K. Meehan, L. J. Romans, J. T. Schofield, D. J. McCleese, W. G. Melbourne, C. L. Thornton, T. P. Yunck, J. R. Eyre, and R. N. Nagatani, Initial results of radio occultation observations of Earth's atmosphere using the Global Positioning System, *Science*, *271*, 1107–1110, 1996.
- Lindal, G. F., J. R. Lyons, D. N. Sweetnam, V. R. Eshleman, D. P. Hinson, and G. L. Tyler, The atmosphere of Uranus: Results of radio occultation measurements with Voyager 2, *J. Geophys. Res.*, *92*, (A13), 14,987–15,001, 1987.
- Marquardt, C., K. Labitzke, C. Reigber, T. Schmidt, and J. Wickert, An assessment of the quality of GPS/MET radio limb soundings during February 1997, *Physics*

Chem. Earth, Part A: Solid Earth and Geodesy, 26, (3), 125–130, 2001.

Martin, J. M., and S. M. Flatté, Intensity images and statistics from numerical simulation of wave propagation in 3-D random media, *Appl. Opt.*, 27, (11), 2111–2126, 1988.

Melbourne, W. G., E. S. Davis, C. B. Duncan, G. A. Hajj, K. R. Hardy, E. R. Kursinski, T. K. Meehan, L. E. Young, and T. P. Yunck, The application of spaceborne GPS to atmospheric limb sounding and global change monitoring, JPL Publication 94-18, Jet Propulsion Laboratory, USA, April 1994.

B. W. Parkinson and J. J. Spilker (Eds.), *Global Positioning System: Theory & Applications*, Amer. Inst. of Aeronauti., 1996.

Reigber, C., H. Lühr, and P. Schwintzer, CHAMP mission status and perspectives, *Suppl. to EOS Transactions, AGU*, 81, (48), F307, 2000.

Reigber, C., H. Lühr, and P. Schwintzer, CHAMP mission status, *Adv. Space Res.*, 30, (2), 129–134, 2002.

Rocken, C., R. Anthes, M. Exner, D. Hunt, S. Sokolovskiy, R. Ware, M. Gorbunov, W. Schreiner, D. Feng, B. Herman, Y.-H. Kuo, and X. Zou, Analysis and validation of GPS/MET data in the neutral atmosphere, *J. Geophys. Res.*, 102, (D25), 29,849–29,866, 1997.

Sokolovskiy, S. V., Modeling and inverting radio occultation signals in the moist troposphere, *Radio Sci.*, 36, (3), 441–458, 2001.

Stensby, J. L., *Phase-Locked Loops*, CRC Press, New York, 1997.

- Thomas, J. B., Signal-processing theory for the TurboRogue receiver, JPL Publication 95-6, Jet Propulsion Laboratory, Pasadena, USA, 1995.
- Tsui, J. B.-Y., *Fundamentals of Global Positioning System Receivers: A Software Approach*, Wiley-Interscience, 2000.
- Vaisala, Upper air systems: RS 80 radiosondes, technical report, Vaisala GmbH, Hamburg, 1989.
- Ware, R., C. Rocken, F. Solheim, M. Exner, W. Schreiner, R. Anthes, D. Feng, B. Herman, M. Gorbunov, S. Sokolovskiy, K. Hardy, Y. Kuo, X. Zou, K. Trenberth, T. Meehan, W. Melbourne, and S. Businger, GPS sounding of the atmosphere from low Earth orbit: Preliminary results, *Bull. Am. Meteorol. Soc.*, 77, (1), 19–40, 1996.
- Wickert, J., C. Reigber, G. Beyerle, R. König, C. Marquardt, T. Schmidt, L. Grunwaldt, R. Galas, T. K. Meehan, W. G. Melbourne, and K. Hocke, Atmosphere sounding by GPS radio occultation: First results from CHAMP, *Geophys. Res. Lett.*, 28, (17), 3263–3266, 2001.

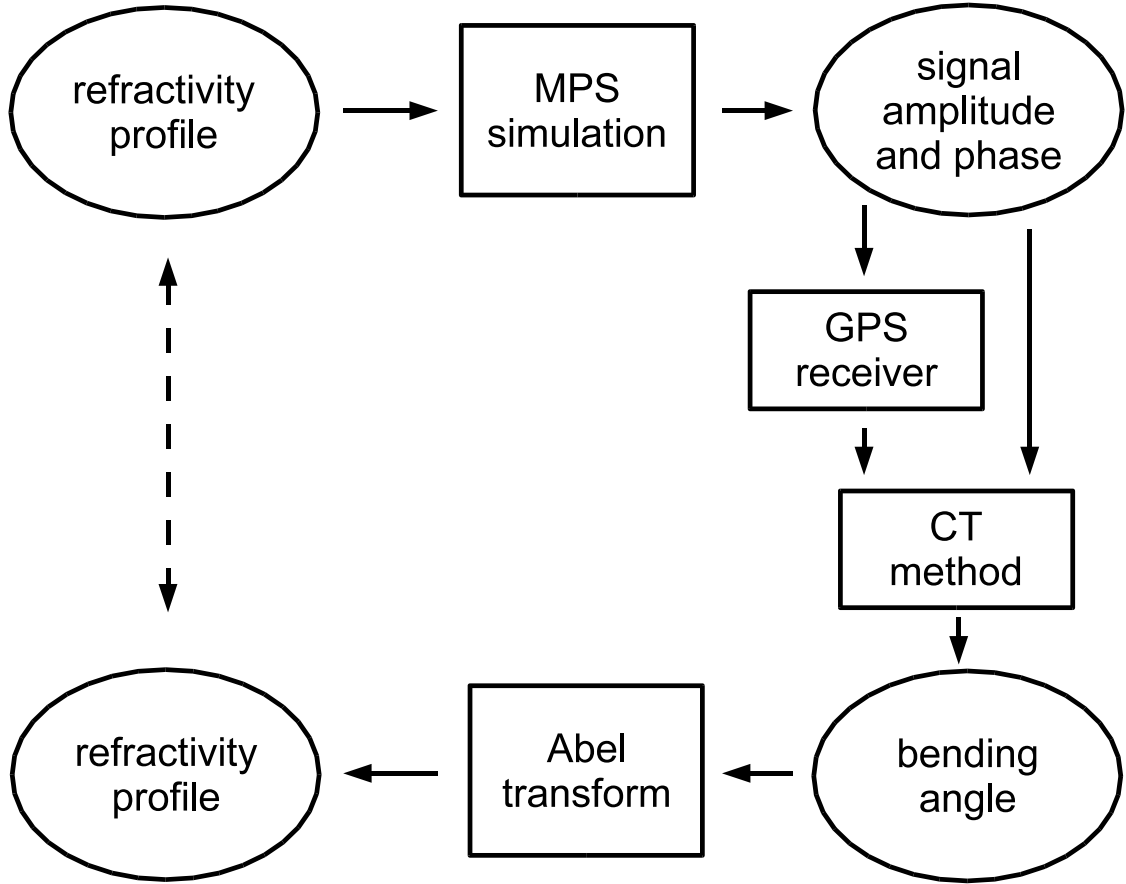


Figure 1. Overview of the simulation procedure. Using the multiple phase screen (MPS) method the atmospheric propagation of a GPS signal based on refractivity profiles is modeled. The generated signal amplitude and phase serves as input to a GPS software receiver. The receiver’s output are converted to bending angle profiles using the canonical transform (CT) method. The simulation loop is closed by Abel-transforming the bending angle profiles into refractivity profiles.

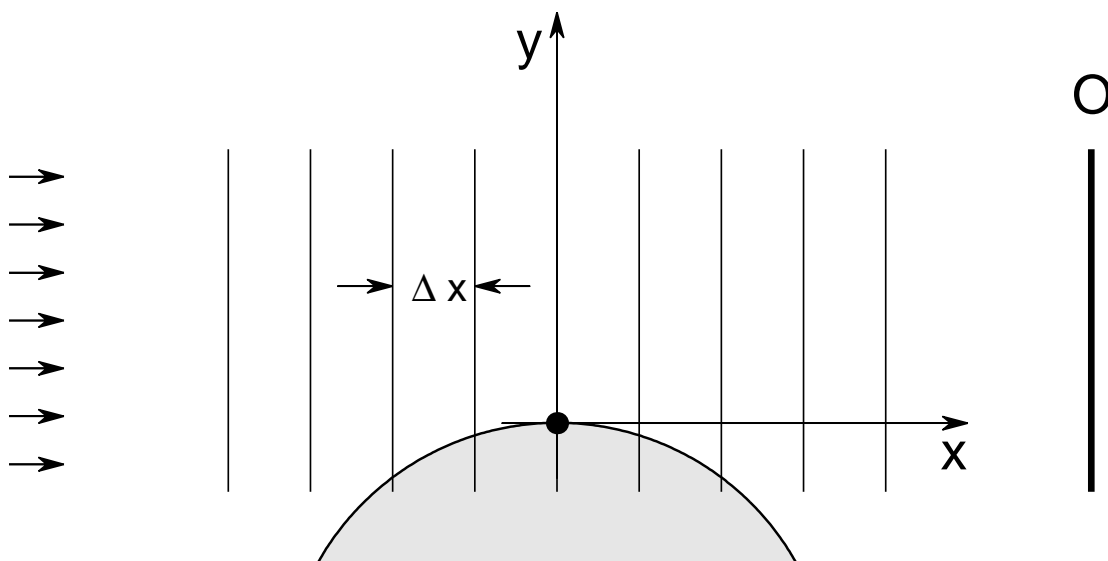


Figure 2. Schematic representation of the multiple phase screen method. The atmosphere is represented by a series of phase screens. A plane electromagnetic wave propagates through the screens from left to right and is detected on observation screen O .

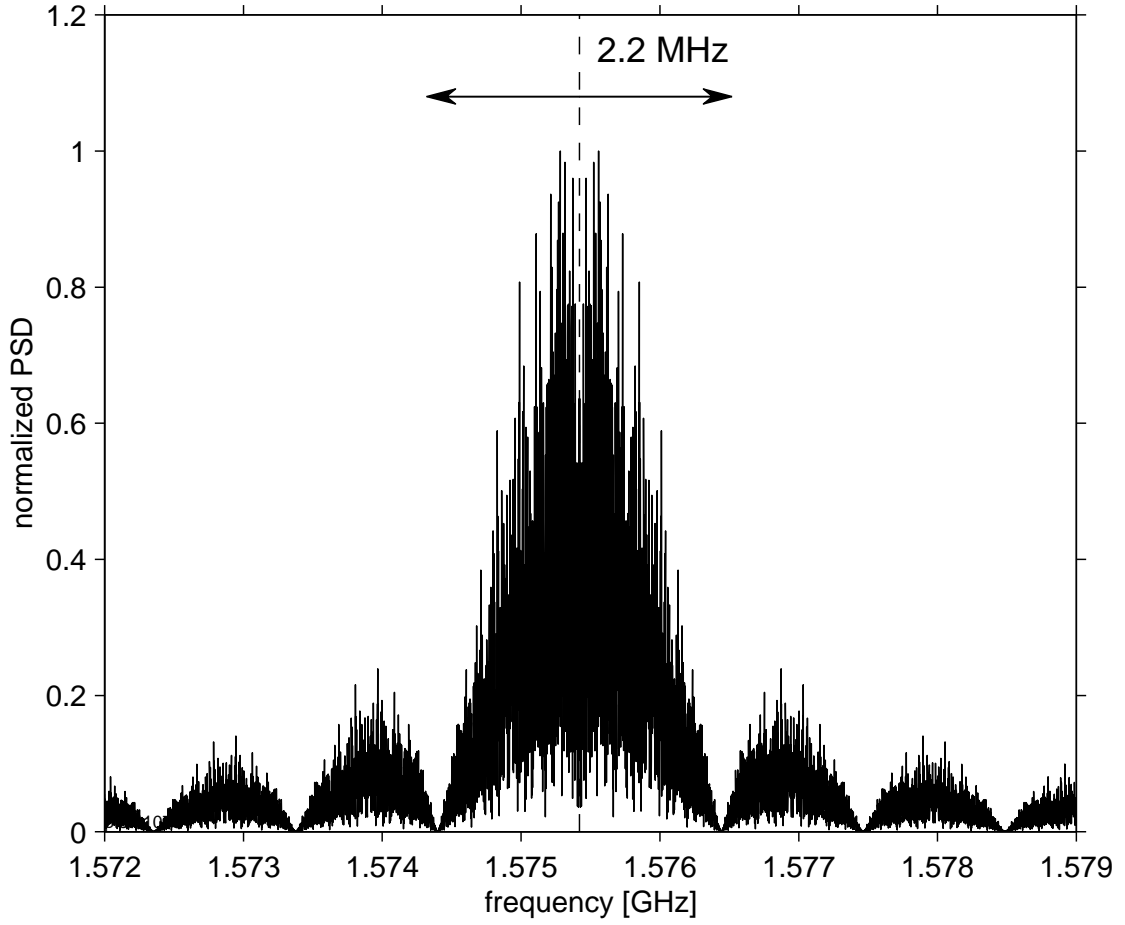


Figure 3. Power spectral density of a C/A-code modulated L1 signal (PRN 17). The carrier frequency of 1.57542 GHz is marked by a dashed line. Note that the spectrum is carrier-free.

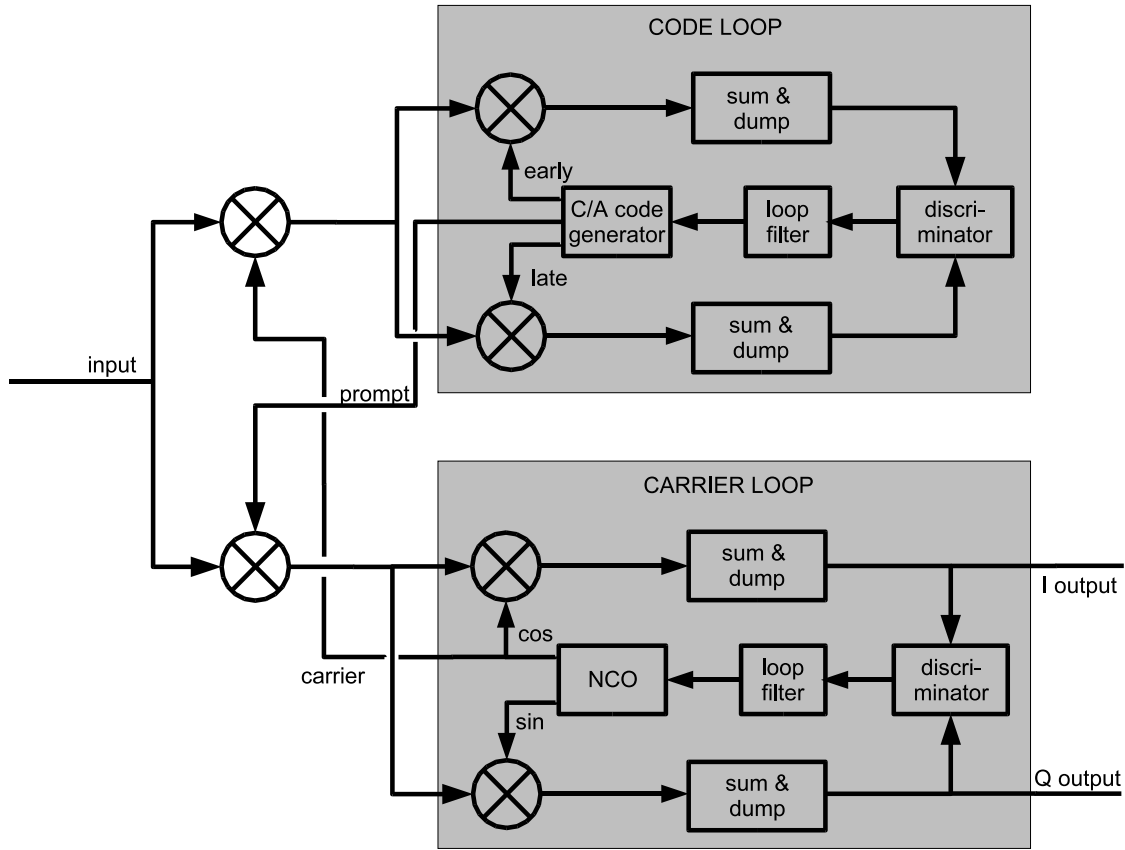


Figure 4. Schematics of code and carrier loop. The carrier phase-locked loop tracks the carrier, the code PLL the code, respectively. The output from the code loop is used to remove the C/A-code modulation from the down-converted signal and, correspondingly, the output from the carrier loop is used to remove the carrier.

Parameter	carrier PLL	code PLL
bandwidth B_n	20 Hz	1 Hz
gain G	2π 200	50
damping ratio ζ	$1/\sqrt{2}$	$1/\sqrt{2}$

Table 1. Carrier and code tracking loop parameters used in the simulation study.

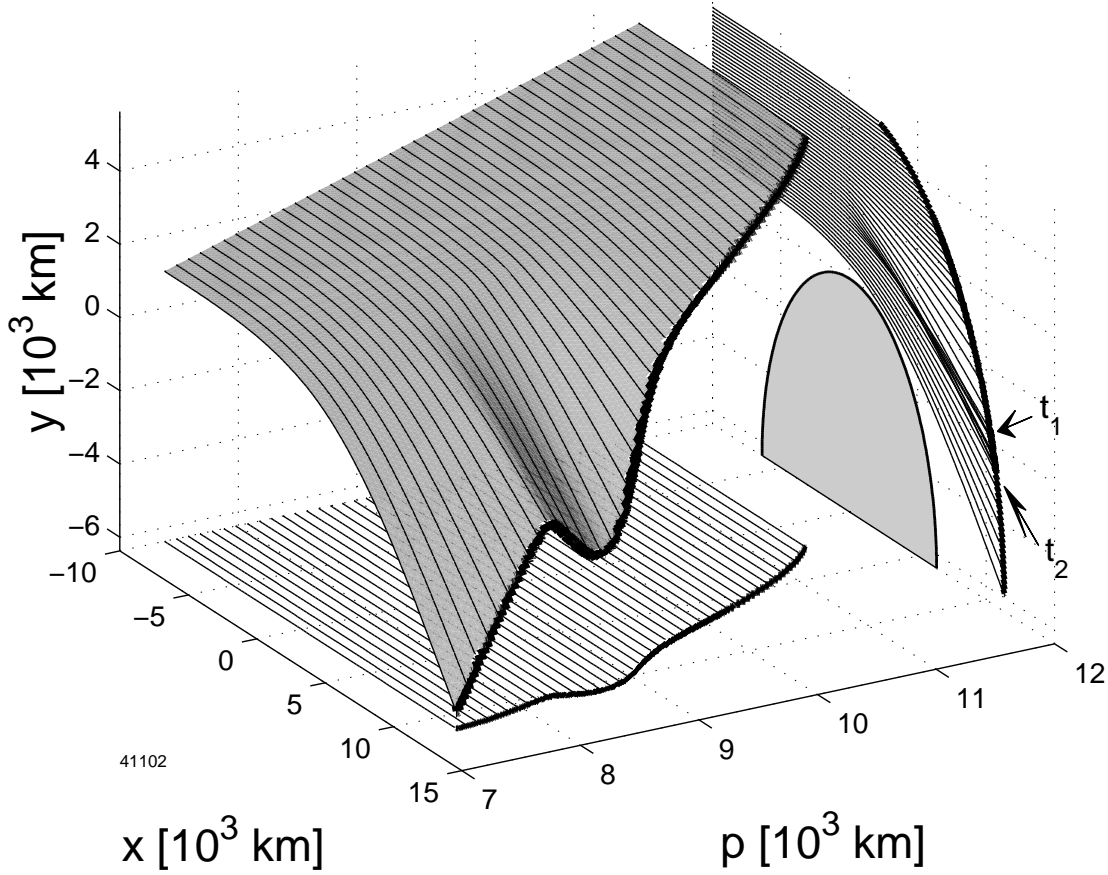


Figure 5. Ray manifold in three dimensional (x, y, p) space. x and y span the occultation plane in geometrical space, p and x form the impact parameter space with p denoting the impact parameter. In this example, the receiver encounters a multipath region between t_1 and t_2 : within this region rays probing the atmosphere on different paths superimpose and interfere with each other. The individual contributions can be separated by transforming the measured signal from geometrical space to impact parameter space (projection onto (p, x) -plane). For details see text. (Figure is not to scale.)

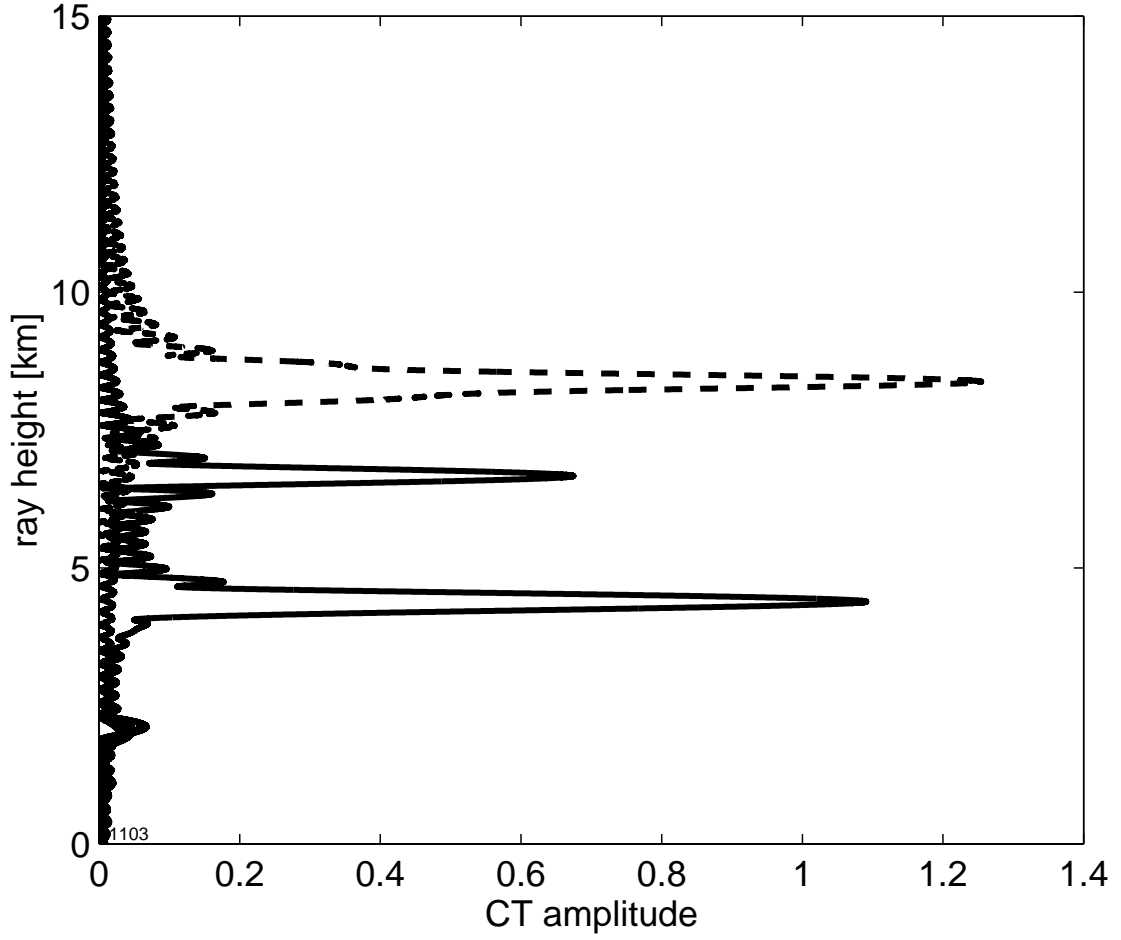


Figure 6. CT-amplitudes for two spatially filtered signals showing the contributions from rays observed between -24 and -26 km on the observation screen (solid line) and between -14 and -16 km (dashed line). The -24 to -26 km range lies within a multipath regions where ray arriving from ray heights of about 6.5 and 4.5 km interfere.

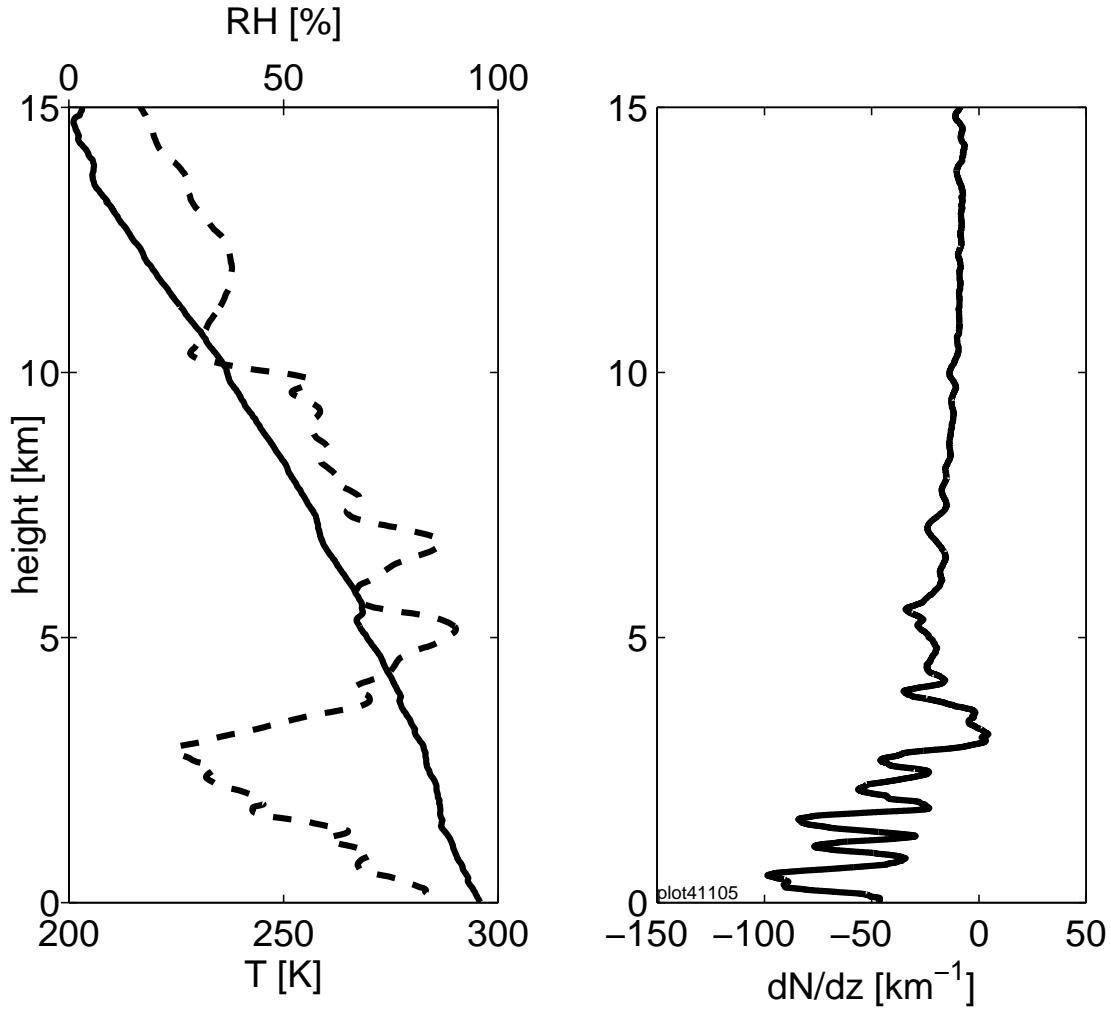


Figure 7. Temperature (solid line) and humidity (dashed line) are plotted in the left panel, the vertical refractivity gradient is shown in the right panel. The profiles are derived from a tropical radiosonde sounding.

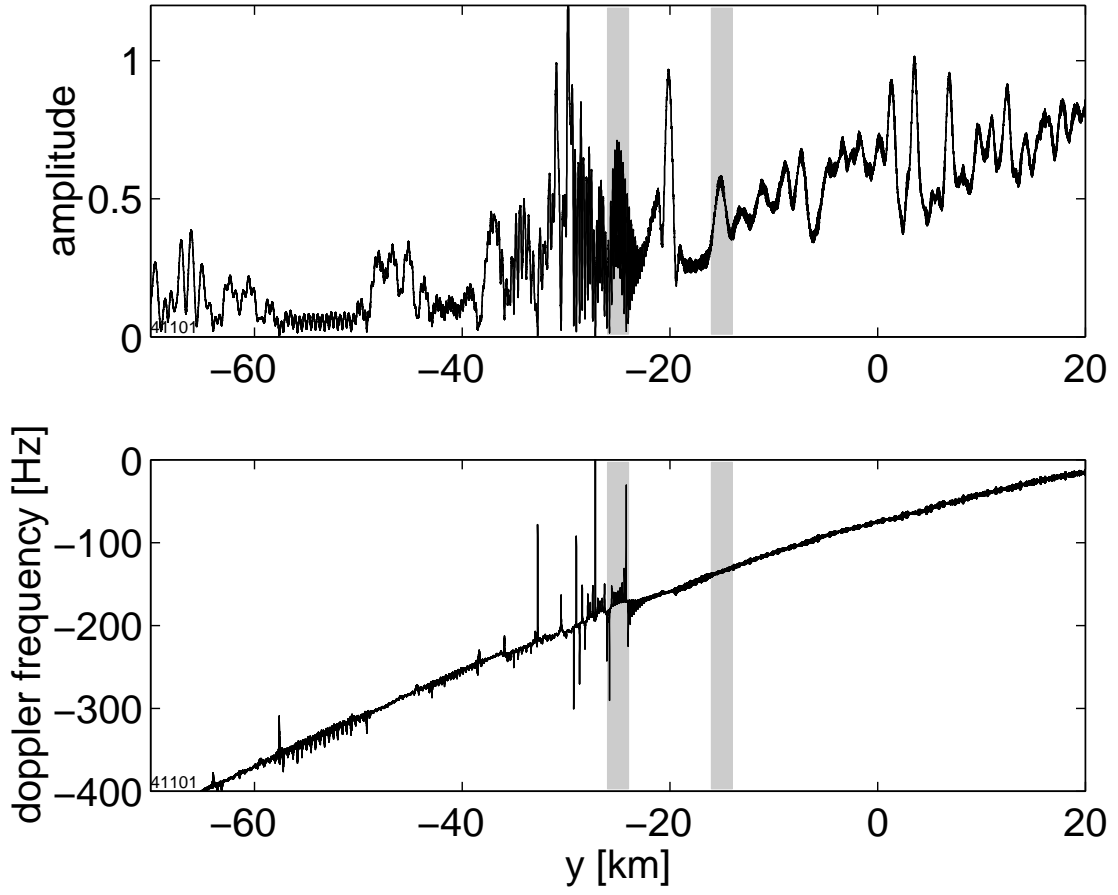


Figure 8. Amplitude (top panel) and Doppler frequency profile (bottom panel) at the carrier frequency of 1.57542 GHz obtained by MPS calculations. The profiles are obtained from the refractivity field plotted in Fig. 7. The observation screen ranges analyzed in Fig. 6 (single path propagation between -14 and -16 km, multipath propagation between -24 and -26 km) are marked in grey.

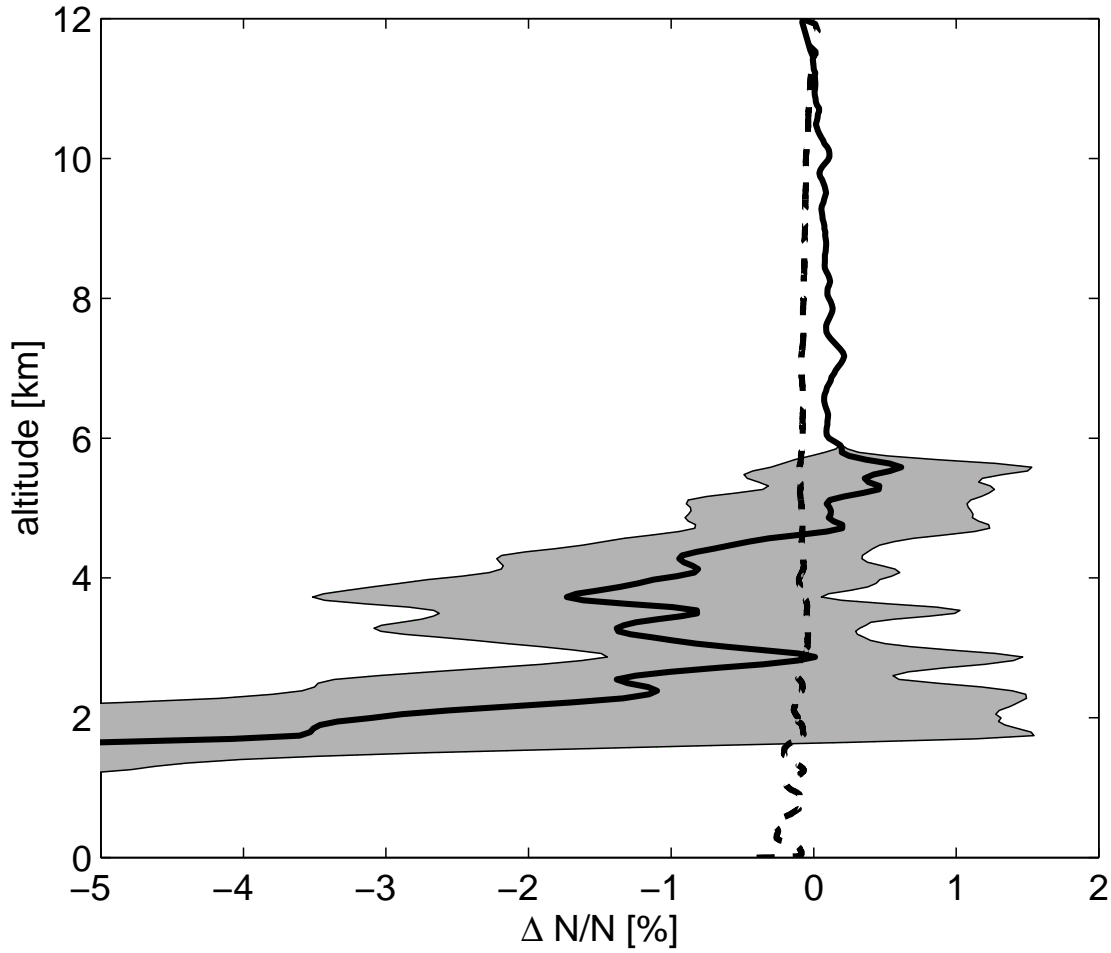


Figure 9. The relative deviation between derived refractivity and the true profile (solid line). Sampling rate is taken to be 50 Hz and a two-quadrant phase detector is used. The grey area marks the 1-sigma standard deviation. The result obtained with an ideal receiver is plotted as a dashed line.

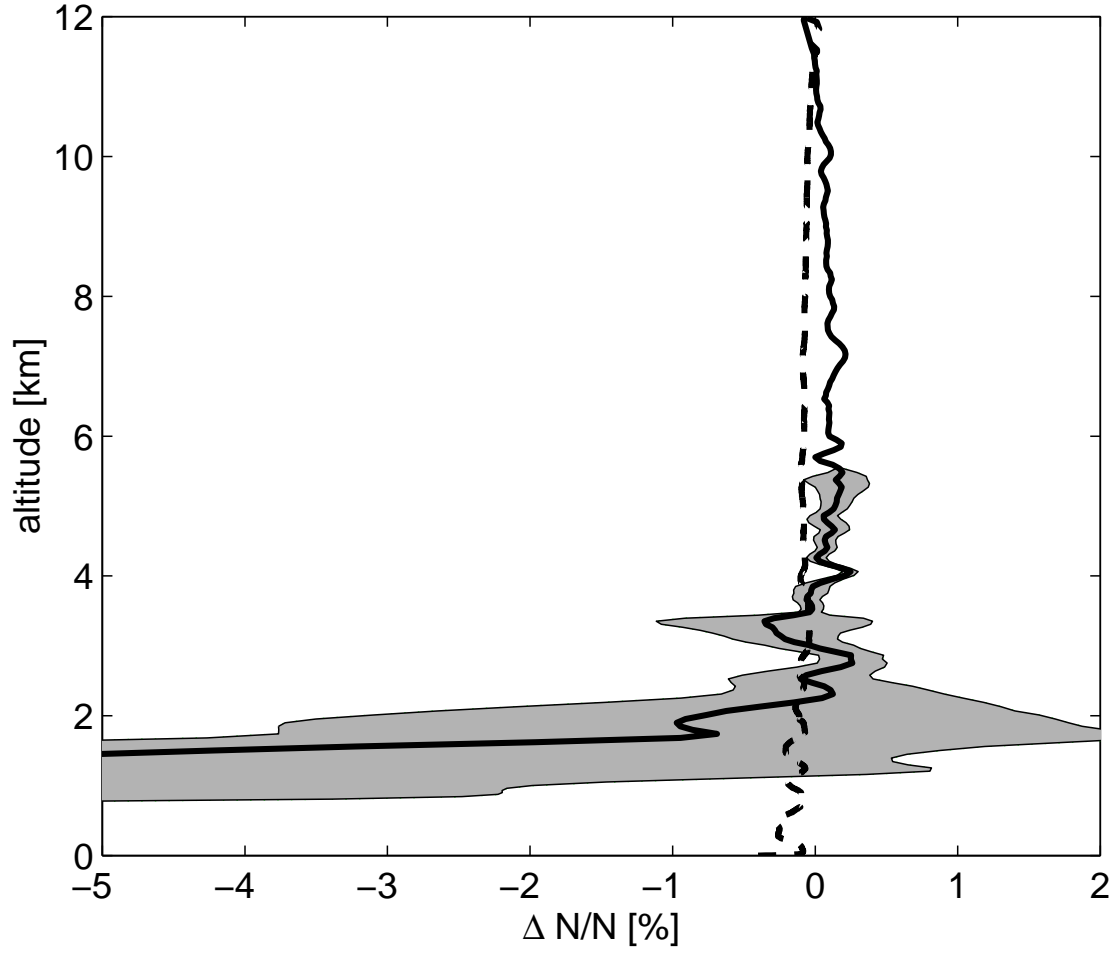


Figure 10. Same as Fig. 9, however, receiver tracking is performed with a four-quadrant phase detector.

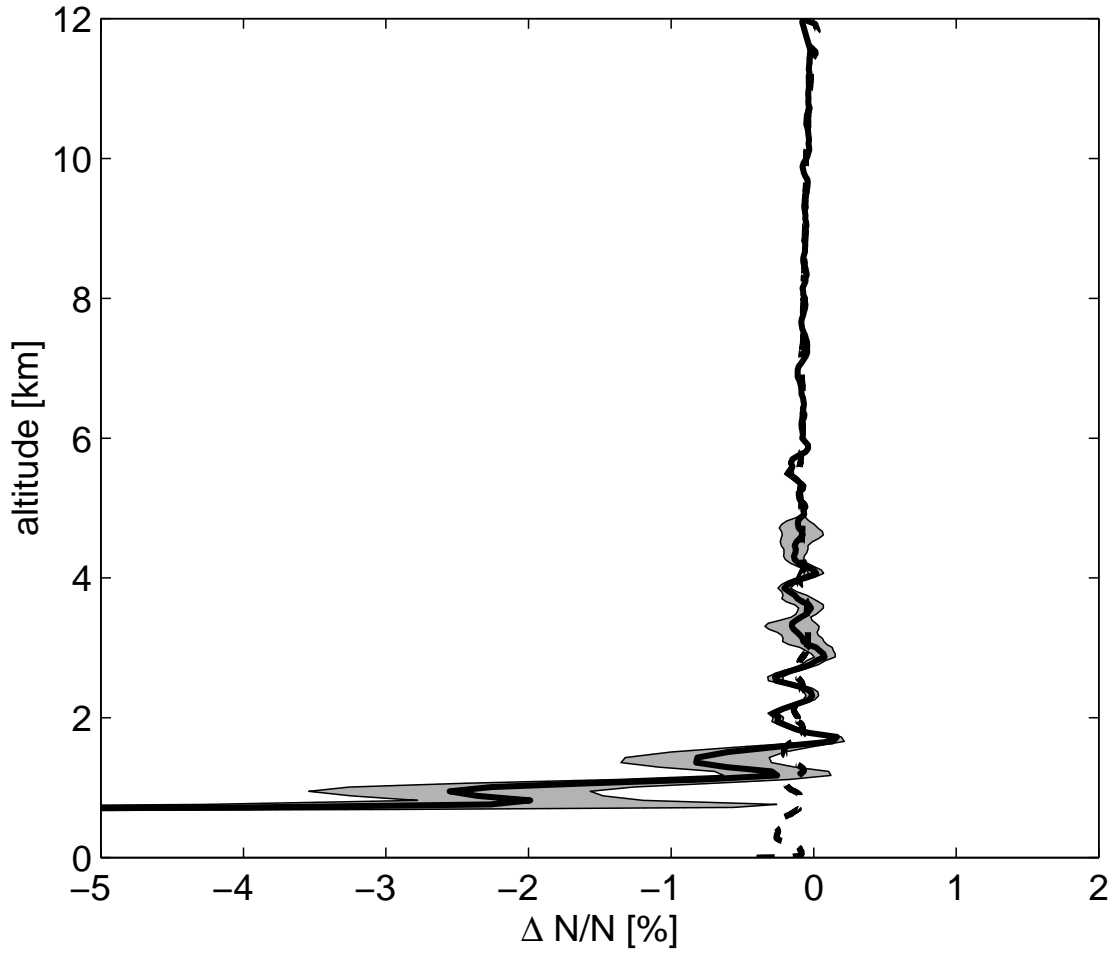


Figure 11. Same as Fig. 10, however, sampling rate is increased to 200 Hz.

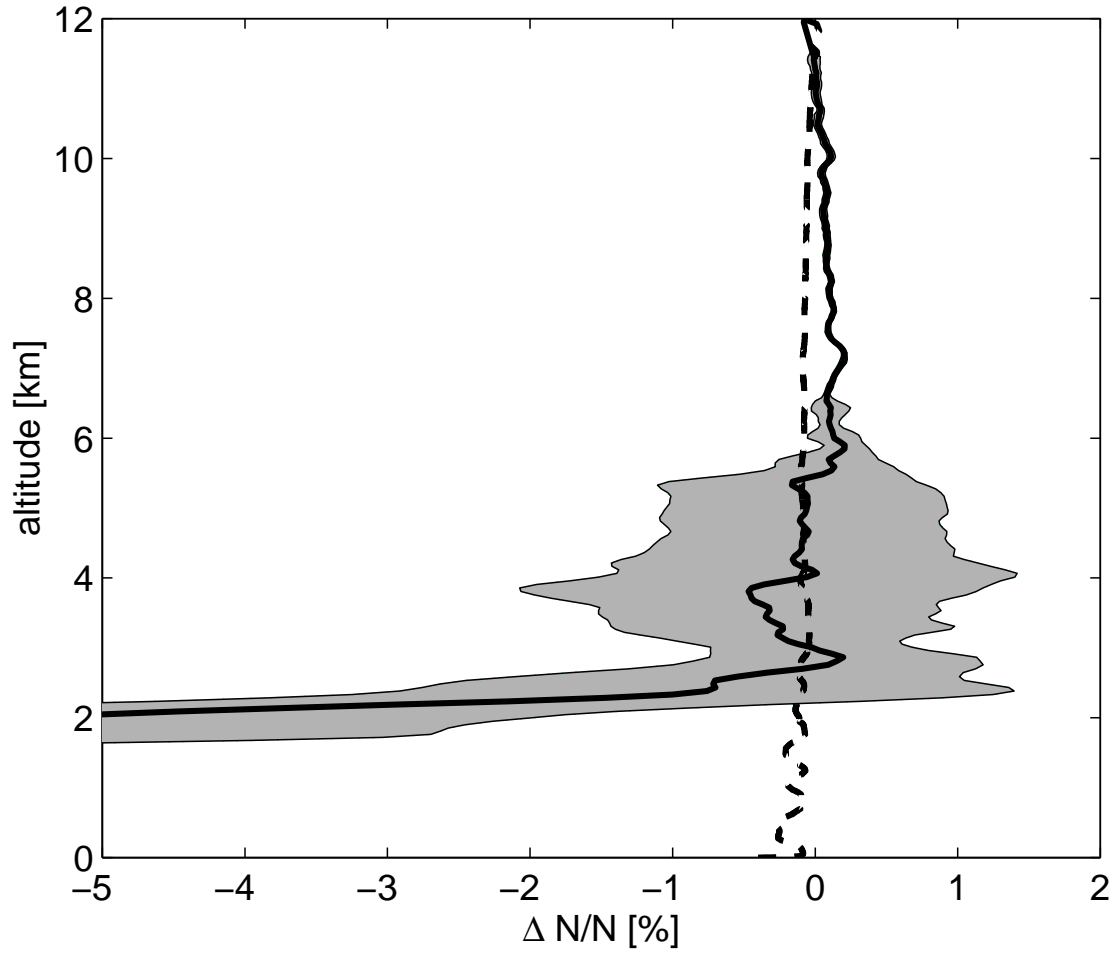


Figure 12. Same as Fig. 11, however, with signal-to-noise ratio lowered from -14 dB down to -24 dB.

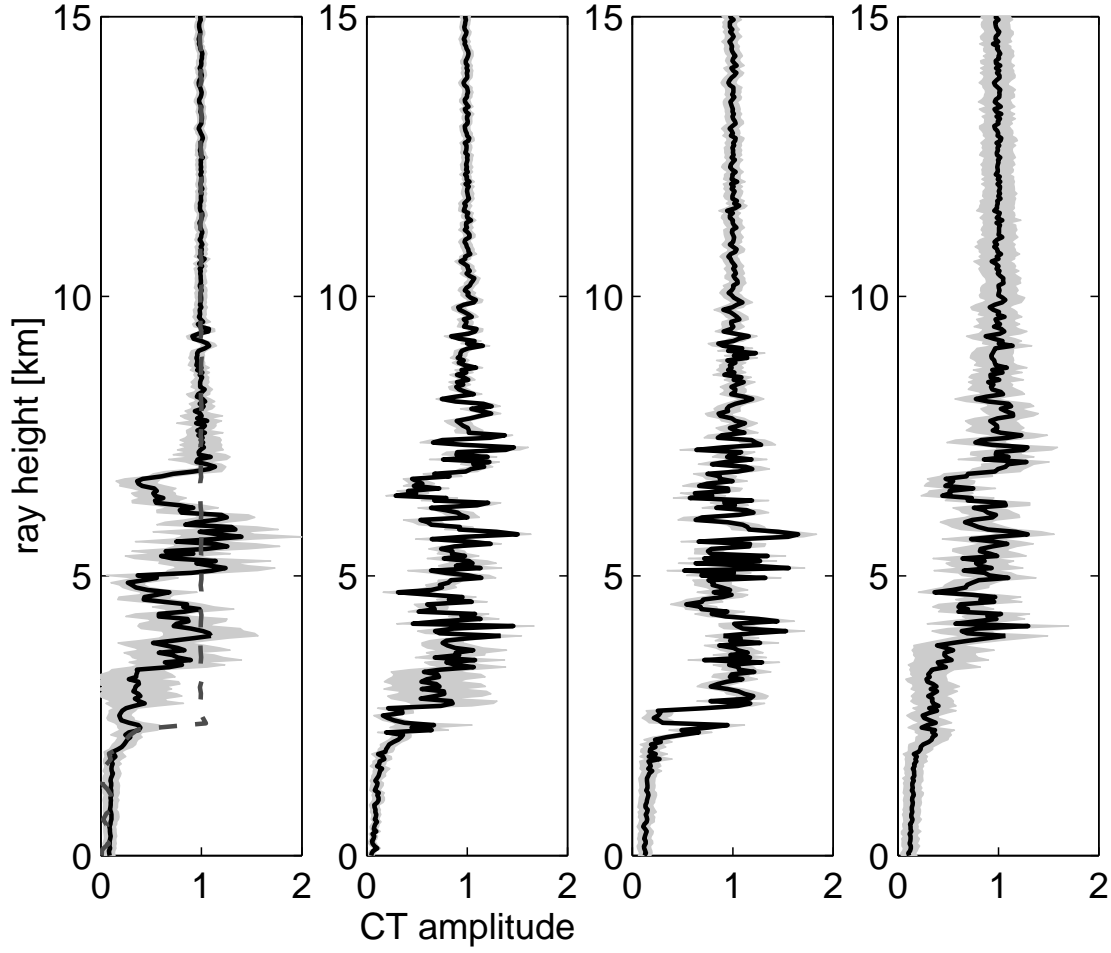


Figure 13. The normalized CT amplitudes corresponding to the simulation results shown in Figs. 9 to 12 (left to right). The $1\text{-}\sigma$ standard deviation is plotted in light grey. The dashed line (left panel) marks the CT-amplitude obtained from the receiver-free simulation.

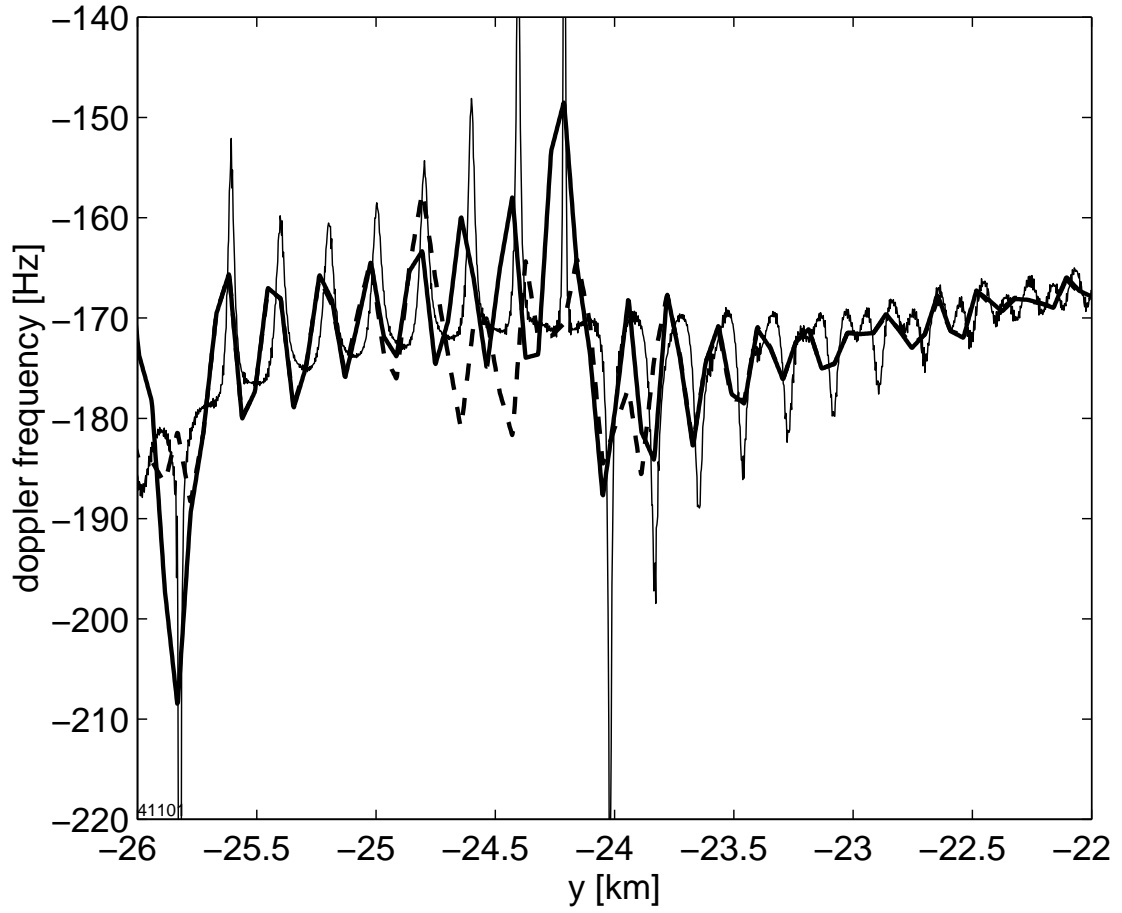


Figure 14. Doppler frequency profile as a function of receiver position on the observation plane. Thin line: true profile, thick solid line: tracking results with four-quadrant phase detector, dashed line: tracking results with two-quadrant phase detector.

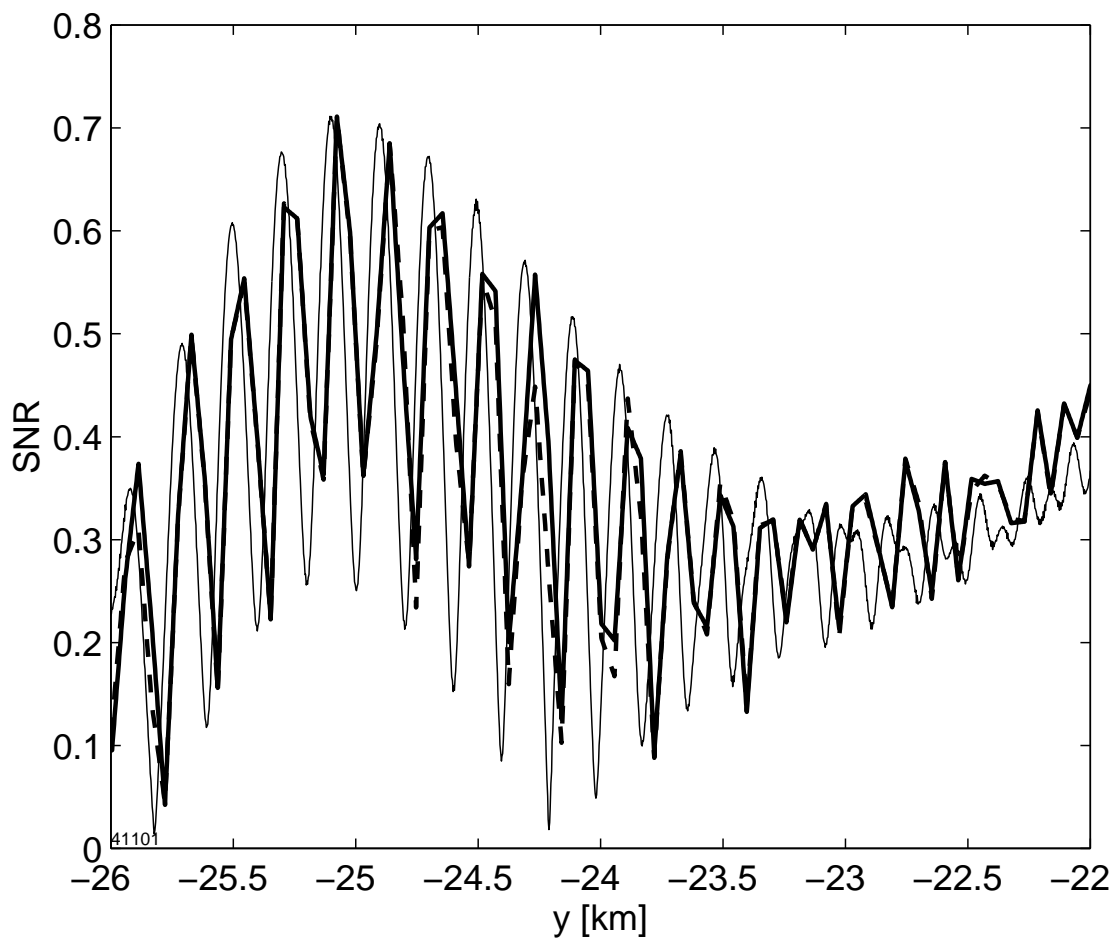


Figure 15. Same as Fig. 14, however showing the corresponding amplitude data.

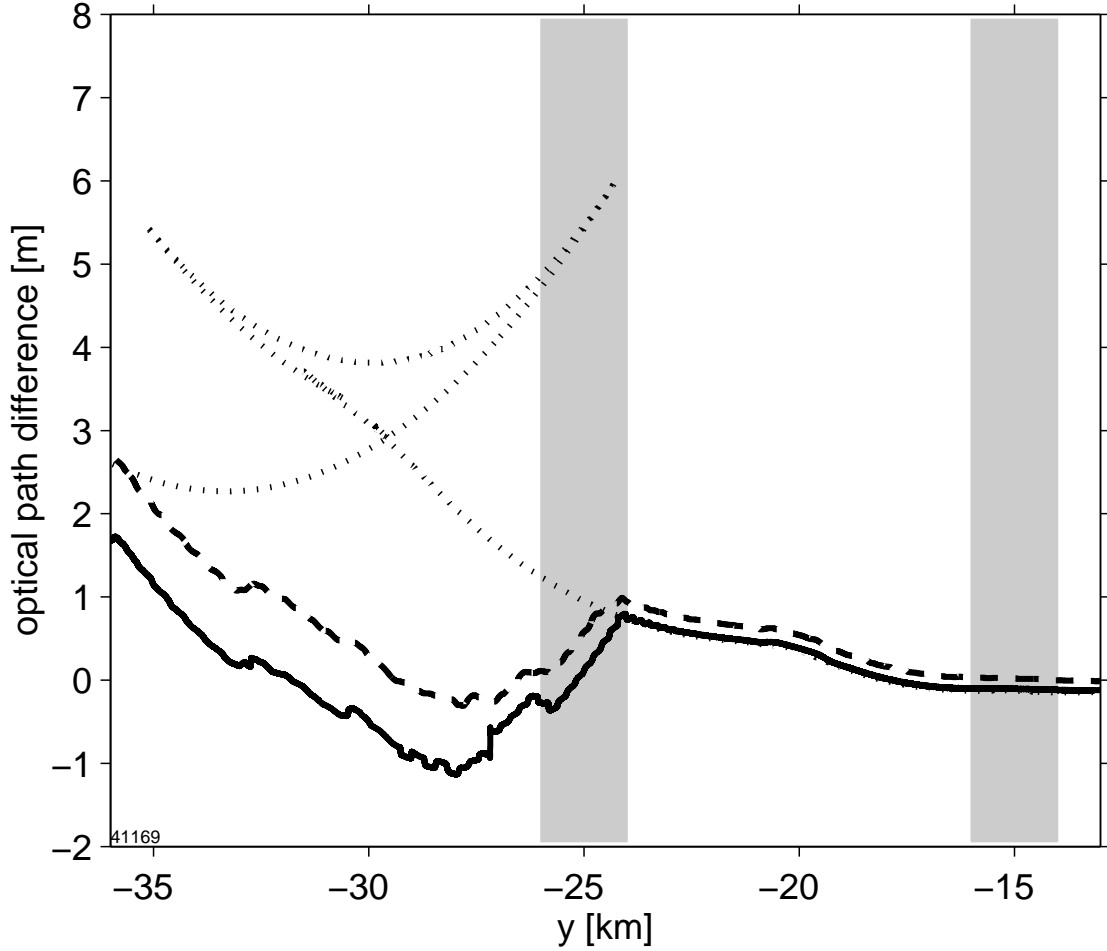


Figure 16. Optical path length differences as a function of screen position y obtained from geometrical raytracing (dotted line), from MPS calculations without receiver processing (solid line) and including receiver tracking (dashed line). Since the optical path increases by about 300 m between $y = -13$ km and $y = -36$ km an offset obtained by fitting a second order polynomial through the MPS solution has been subtracted. The observation screen ranges analyzed in Fig. 6 (single path propagation between -14 and -16 km, multipath propagation between -24 and -26 km) are marked in grey.